1   Total Column Ozone Trends from the NASA Merged Ozone Time Series 1979 to 2021 Showing Latitude
2                   Dependent Ozone Recovery Dates (1994 to 1998)

3              Jay Herman[1], Jerald Ziemke[2], and Richard McPeters[3]

[1]University of Maryland Baltimore County, Baltimore Maryland USA

[2]Morgan State University, Baltimore Maryland, USA

[3]NASA Goddard Space Flight Center, Greenbelt, Maryland, USA

Corresponding Author:   Jay Herman     Herman@umbc.edu

17   **Abstract**

18   Monthly averaged total column ozone data $\Omega_{MOD}(t,\theta)$ from the NASA Merged Ozone Data set

19   (MOD) were examined to show that the latitude-dependent, $\theta$, ozone depletion turnaround dates $T_A(\theta)$

20   range from 1994 to 1998. $T_A(\theta)$ is defined as the approximate date when the zonally averaged ozone

21   ceased decreasing. $\Omega_{MOD}$ data used in this study were created by combining data from Solar

22   Backscattered Ultraviolet instruments (SBUV/SBUV-2) and the Ozone Mapping and Profiler Suite (OMPS-

23   NP) from 1979 to 2021. The newly calculated systematic latitude-dependent hemispherically

24   asymmetric $T_A(\theta)$ shape currently does not appear in the suite of chemistry-climate models that are part

25   of the Chemistry-Climate Model Validation Activity CCMVal, which combines the effects of

26   photochemistry, volcanic eruptions, and dynamics in their estimate of ozone recovery. Trends of zonally

27   averaged total column ozone in percent per decade were computed before and after $T_A(\theta)$ using two

28   different trend estimate methods that closely agree, Fourier Series Multivariate Linear Regression and

29   linear regression on annual averages. During the period 1979 to $T_A(\theta)$ the most dramatic rates of SH

30   ozone loss were $P_D$ = -10.9 ± 3 % per decade at 77.5$^O$S and -8.0±0.9% per decade at 65$^O$S, which is about

31   double the NH rate of loss of $P_D$ = -5.6±4 %/decade at 77.5$^O$N and 4.4±1%/decade at 65$^O$N for the period

32   1979 to $T_A(\theta)$. After $T_A(\theta)$, there has been an increase at 65$^O$S of $P_D$ = 1.6±1.4% per decade with  smaller

33   increases from 55$^O$S to 25$^O$S and a small decrease at 35$^O$N of -0.4±0.3 %/decade. Except for the Antarctic

34   region, there only has been a small recovery in the Southern Hemisphere toward 1979 ozone values and

35   almost none in the Northern Hemisphere.

36

37

38

39    **1.0 Introduction**

40    Ozone is a photolytically produced, photochemically destroyed, and dynamically distributed
41    atmospheric gas that plays a crucial role in protecting the planet from harmful ultraviolet (UV) radiation
42    from the sun. The atmospheric presence of bromine and the release of chlorine from the UV
43    dissociation of man-made chemicals, such as chlorofluorocarbons (CFCs), can break down the ozone
44    layer at all latitudes. This is especially the case in the Antarctic region where heterogeneous chemistry
45    on and within ice crystals and liquid droplets (Tritscher, et al., 2021) in polar stratospheric clouds PSCs
46    have a strong effect on the destruction of ozone during September and October (WMO, 2022; Tritscher,
47    et al., 2021; Solomon et al., 1986; 1999; 2016; Crutzen and Arnold, 1986; Khosrawi et al., 2011).  As the
48    sun rises in Spring, chemically active nitrogen oxides, chlorine and bromine are released causing the
49    ozone hole to develop within the region enclosed by the polar vortex winds. The weak levels of sunlight
50    are sufficient to initiate and maintain the catalytic ozone loss photochemistry. In November and
51    December, the isolating polar vortex winds break down and the Antarctic ozone hole region back fills by
52    air exchange from southern mid-latitudes causing $T_A(35^OS – 65^OS)$ to be delayed compared to the
53    Northern Hemisphere NH mid-latitudes. The recurring annual ozone hole event triggered international
54    action to limit the production and use of ozone-depleting substances (ODS) under the Montreal
55    Protocol, which has been successful in reducing the emission of these substances, slowing down the
56    depletion of the ozone layer globally, leading to a partial recovery in the Antarctic ozone hole region
57    (Solomon et al., 2016; Strahan and Douglass 2018). After the mid-1990s, several studies have reported
58    an increase in total column ozone (TCO), particularly in the mid to high latitudes of the Southern
59    Hemisphere, as well as a reduction in the size and depth of the Antarctic ozone hole starting in the late
60    1990s (Solomon et al., 2016; Stone et al., 2018; 2021, Weber et al., 2022).

61    The cessation of ozone decrease was first observed in the mid-1990s when satellite data showed a
62    stabilization and slight increase in ozone concentrations in the Antarctic ozone hole region. However,
63    the recovery was not significant enough to be considered a trend at that time (Strahan and Douglass
64    2018). In the early 2000s, further analysis of satellite and ground-based data showed that the rate of
65    ozone depletion had slowed down. After the mid-1990's, the cessation of ozone depletion has been
66    most evident in the Southern Hemisphere SH polar region, where ozone depletion had been most
67    severe. Ozone recovery has been slow or non-existent at other latitudes. Recently, Weber et al. (2022)
68    showed reduction in ozone at all latitudes prior to 1995 and reported positive statistically significant
69    TCO trends from 1996-2020 at southern middle and high latitudes, and over the SH polar cap in
70    September. When dynamical terms were included in the regression, small positive trends were near the
71    2-standard deviation $2\sigma$ threshold at northern mid- and high-latitudes, with no trend detected in the
72    tropics or over the NH polar cap.

73    Despite the success of the Montreal Protocol (Velders and Andersen, 2018), ozone concentrations
74    continue to fluctuate, driven by natural and anthropogenic factors, such as, changes in solar radiation,
75    stratospheric circulation, global warming, volcanic activity, and changing emissions of ozone precursors
76    (Dameris and Baldwin, 2012; Weber et al., 2022). The discussion by Dameris and Baldwin (2012)
77    explored possible effects of climate change on the dynamics of the atmosphere affecting ozone as ODSs
78    change, and particularly the change in the Brewer-Dobson circulation (Brewer, 1949; Dobson et al.,

79    1926) that transports ozone from an upwelling in the equatorial region into the stratosphere and to
80    downwelling into mid- and high-latitudes.

81    A comparison of several atmospheric chemistry and dynamics model studies as part of the Chemistry-
82    Climate Model Validation (CCMVal) Activity (Eyring, et al. 2010a, their Fig. 1; Dhomse et al., 2018;
83    Robertson et al., 2023) generally predict an ozone turnaround date $T_A$ in the year 2000 with no
84    systematic latitude dependence. In particular, Robertson et al. (2023) shows latitude dependence of
85    long-term ozone recovery, but $T_A$ = 2000 for all cases. Quoting from the Sparc Report No. 5 (Eyring, et al.
86    2010b), "Common systematic errors in CCM results include: tropical lower stratospheric temperature,
87    water vapor, and transport; response to volcanic eruptions", which may affect the determination of $T_A$
88    as a function of latitude and time. The results of this study may provide a convenient metric for model
89    validation compared to $T_A$ derived from ozone data.

90    This study will estimate new latitude dependent ozone recovery dates, or more accurately the dates of
91    cessation of ozone decrease, $T_A(\theta)$ ranging from 1994 (equatorial region and $60^O$N to $70^O$N) to 1998
92    ($60^O$S – $80^O$S). The calculated $T_A(\theta)$ and ozone trends (%/decade) include the effects of volcanic
93    eruptions such as Mt. Pinatubo in 1991, dynamics, and atmospheric temperature changes. Ozone data
94    used in this study are a subset of the Merged Ozone Data MOD set $\Omega_{MOD}(t)$ (1970 – 2021) starting in
95    1979 with the Nimbus-7 SBUV (Solar Backscattered Ultraviolet) satellite instrument. From 1979 to 2021,
96    the MOD data set was created by combining data from Solar Backscattered Ultraviolet instruments
97    (SBUV/SBUV-2) and the Ozone Mapping and Profiler Suite (OMPS-NP). Methods of calculating trends
98    from time series data are essential in the analysis of environmental and climate-related data. Here, we
99    discuss two independent methods to estimate linear trends: 1) linear regression of annual averaged
100   data and 2) Fourier time series decomposition or multivariate linear regression MLR (Ziemke et al.,
101   2019) are discussed below. The two methods are compared and shown to give nearly identical results
102   over their mutual latitude range of validity, $65^O$S to $65^O$N. The MLR method is not used in the regions
103   poleward of the Arctic and Antarctic circles that have latitude dependent extended winter polar night.
104   The advantage of the MLR method (Eq. 1), or that in Weber et al, 2002, is that it can be used to estimate
105   the effects of its individual components, while the annual average method can be used in the polar
106   regions to estimate sun lit ozone trends where there is latitude dependent extended winter night.

107   **1.1 The Merged Ozone Data Set MOD**

108   Figure 1 (left panel) shows the MOD zonally averaged $\Omega_{MOD}$ TCO data (Frith et al., 2014; 2020) set as a
109   function of latitude ($5^O$ latitude bands from $77.5^O$S to $77.5^O$N) and time (January 1979 to December
110   2021). Part of the Antarctic ozone hole ($75^O$S to $80^O$S) is shown (blue color), and the high latitude
111   maxima, North and South, (red color), with low values in the equatorial region. Figure 1 (right panel)
112   shows the 42-year zonal and time averaged ozone amounts and the maxima and minima annual
113   envelopes as a function of latitude. Figure 1 shows the asymmetry in the monthly and zonally averaged
114   ozone data between the hemispheres, with the Northern Hemisphere NH having more ozone than the
115   Southern Hemisphere SH at corresponding latitudes. Part of the asymmetry is driven by the Spring
116   Antarctic ozone hole backfilling in the SH summer.
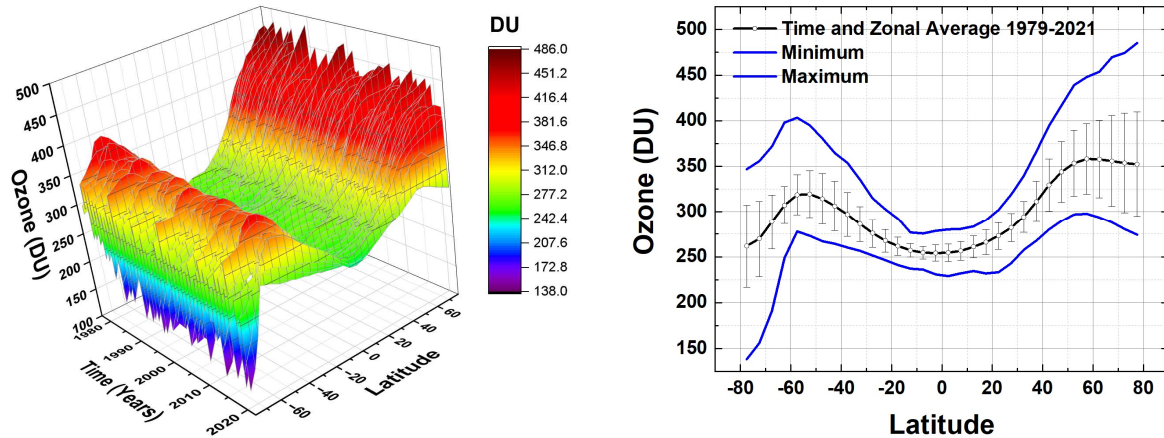
Fig. 1 Left: The zonally and monthly averaged $\Omega_{MOD}$ data set 1979 – 2021 and -77.5$^O$ to 77.5$^O$. Right: Time and zonal averaged ozone and its maxima and minima 1979 – 2021. Error bars are 1 standard deviation ±1σ.

117    $\Omega_{MOD}(t,\theta)$ provides a global view of ozone levels needed to track changes in ozone concentrations over
118    time t for each latitude band θ. The SBUV and OMPS-NP series of satellite instruments form the longest
119    (1979 to 2022) continuous global ozone $\Omega_{MOD}(t,\theta)$ data record from a single instrument type. Merged
120    ozone retrievals from the individual instruments use the version 8.7 retrieval algorithm (described by
121    Weber et al., 2022) as an extension of the version 8.6 algorithm (Bhartia et al., 2013; McPeters et al.,
122    2013; DeLand et al., 2012; Frith et al., 2017) specifically designed to improve cross calibrations between
123    the later SBUV-type instruments in MOD starting from NOAA-16 in 2000. There were no external
124    adjustments made to the ozone retrieval except for small high-altitude (> 35 km) diurnal corrections to
125    account for different measurement times between satellites and varying measurement time of day as
126    individual satellite orbits slowly drift in equator crossing time. These adjustments are very minor in TCO
127    (Frith, personal communication). Data from each instrument are selected based on quality criteria
128    outlined in Frith et al. (2014; 2020) and the data are averaged during periods when more than one
129    instrument was operational. The $\Omega_{MOD}(t,\theta)$ are available as a function of latitude and month,
130    https://acd-ext.gsfc.nasa.gov/Data_services/merged/.
131
132    Analysis of the long-term ozone time series has been looked at extensively with references given in
133    Weber et al., 2022. Methods for estimating trends from an oscillating time series with several distinct
134    periodicities are well known (Ziemke et al., 2019; Stolarski et al. 1991;1992, Herman et al., 1993). For
135    ozone, one of the difficulties in trend estimation is that the early part of the time series shows a strong
136    ozone decrease at all latitudes that continued until the mid-1990s and then flattens out and shows
137    almost no recovery thereafter toward 1979 values.  The $\Omega_{MOD}$ time series has been used extensively in
138    ozone assessments and State of the Climate reports (e.g., WMO, 2022) and was recently compared to
139    several other merged total ozone records in Weber et al. (2022). The validity of the $\Omega_{MOD}$ time series for
140    estimating ozone trends was further checked (See Appendix Figs. A1 to A3) in this study by showing
141    detailed comparisons between the deseasonalized $\Omega_{MOD}$ time series with the deseasonalized MLS
142    (Microwave Limb Sounder) overlapping stratospheric ozone time series (2005 to 2023).

143     **2.0 Trend Estimates from the MOD Ozone Data**

144     Multivariate Linear Regression MLR is a Fourier based method for analyzing atmospheric time series
145     data that decomposes the time series into its component parts, including trend, quasi-biennial
146     oscillation QBO, solar cycle, ENSO (El Nino Southern Oscillation), seasonality, and noise resulting in a
147     trend estimate and 2-standard deviation $2\sigma$ uncertainty estimates (Ziemke et al., 2019). Calculated $2\sigma$
148     uncertainties for the MLR trends include a first order autoregressive adjustment applied to the derived
149     residuals (Weatherhead et al., 1998).

150     Linear trend estimates for the long-term changes in $\Omega_{MOD}(t, \theta_i)$ globally and as a function of latitude $\theta_i$
151     have been obtained using the multivariate linear regression (MLR) model (e.g., Randel and Cobb, 1994,
152     and references therein). Trends $B(\theta_i)$ were determined for $\Omega_{MOD}(t, \theta_i)$ using Eqns. 1 and 2.
153

$$\Omega_{MOD}(t, \theta_i) = A(\theta_I\,t) + B(\theta_I,t)\cdot t + C(\theta_I,t)\cdot QBO_1(t) + D(\theta_I,t)\cdot QBO_2(t) + \qquad\qquad (1)$$
$$E(\theta_I,t)\cdot ENSO(t) + F(\theta_I,t)\cdot Solar(t) + R(t, \theta_I)$$

154
155     where t is the month index (t=1 to 516 months with data for 1979–2021), $A(\theta_i\,t)$ is the seasonal cycle
156     coefficient, $B(\theta_i,t)$ is the trend coefficient, $C(\theta_I,t)$ is the first  empirical orthogonal function (EOF) QBO
157     coefficient, $D(\theta_I,t)$ is the second EOF QBO coefficient, both representing the major components of
158     the QBO variability, $E(\theta_I,t)$ is the ENSO coefficient, $F(\theta_I,t)$ is the solar cycle coefficient, and R(t) is the
159     residual error time series.  The F10.7 cm solar flux monthly time series is used for the Solar(t) proxy, first
160     and second leading EOF QBO monthly time series proxies $QBO_1(t)$ and $QBO_2(t)$ are used for the QBO
161     component (Wallace et al., 1993), and Nino 3.4 (Oldenborgh *et al* 2021) is used for ENSO(t) (Nino 3.4:
162     https://www.ncei.noaa.gov/access/monitoring/enso/sst). $QBO_1(t)$ and $QBO_2(t)$ are nearly orthogonal
163     (correlation coefficient approximately zero) oscillating time series based on data with approximately a
164     2.3-year periodicity.  $A(\theta_I,t)$ involves 7 fixed constants while $B(\theta_I,t)$ (and all other remaining coefficients)
165     involves 5 fixed constants for each $\theta_I$.  The harmonic expansion for A(t) (similar for the other
166     coefficients) is (Eqn. 2).
167

$$A(t) = a(0) + \sum_{p=1}^{3}\left[a(p)\cos(2\pi pt/365) + b(p)\sin(2\pi pt/365)\right] \qquad (2)$$

168
169     where a(p) and b(p) are constants. Statistical uncertainties for A(t) and $B(\theta_i)$ were derived from the
170     calculated statistical covariance matrix involving the variances and cross-covariances of the constants
171     (e.g., Guttman et al., 1982; Randel and Cobb, 1994).
172
173     In this study the Locally Weighted Scatterplot Smoothing Lowess(f) least-squares technique is used to
174     reduce oscillations in the time series data and to estimate $T_A(\theta)$ where f = the fraction of data averaged
175     together (Cleveland, 1979 and Cleveland and Devlin, 1988).

176
177
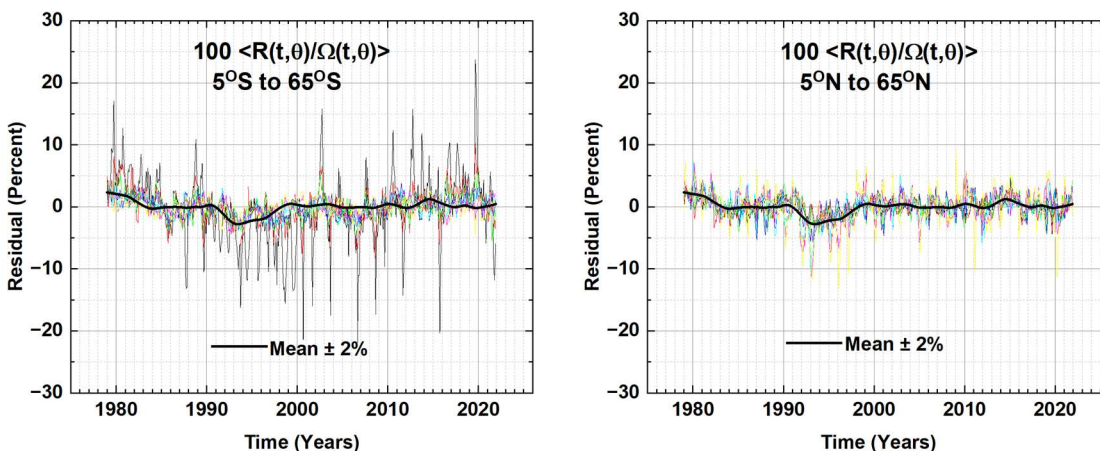
Fig. 2 The latitude average residual term from Eq. 1 in percent 100 <R(t,q$_i$)/W$_{MOD}$(t,q$_i$)> The black line is the Lowess(0.1) fit (Cleveland, 1979) to the R(t,q) with an average error estimate of ±2%. The light-colored lines are each latitude's R(t,q) in a hemisphere $0^O < \theta < 65^O$.

178

179     The latitude average residual R(t) in percent of the MOD ozone amount (100 <R(t,$\theta_i$)/ $\Omega_{MOD}$(t,$\theta_i$)>) is shown

180     in Fig. 2 for the SH and NH as an indication of how well Eq 1 is able to fit the $\Omega_{MOD}$(t,$\theta_i$) time series.

181

182     The SH R(t,$\theta$) is more variable than the NH with the largest variations arising in the 55$^O$S and 65$^O$S latitude

183     bands. On average Eq. 1 fits the original data $\Omega_{MOD}$(t,$\theta_i$) to within ±2%.

184

185     The linear deseasonalized trend results B($\theta_i$) are obtained for 14 latitude bands $\theta_i$ (centered on 65$^O$S to

186     65$^O$N). The latitudinal trends P$_D$($\theta_i$) are expressed in %/Decade given by Eq. 3, where the denominator D

187     is either the time average <$\Omega$> of the area weighted global ozone average (Fig 1) or the time average D($\theta_i$)

188     = < $\Omega_{MOD}$(t, $\theta_i$)> for each latitude band over the considered period. The whole year period considered is

189     1979 – 2021.

190

$$P_D(\theta_i) = 1000\ B(\theta_i)\ /D(\theta_i) \quad\quad (\% \ / \ Decade) \quad\quad\quad (3)$$

191

192     In the second method, the trend is estimated using annual integrals (annual averages) that remove the

193     seasonality and other short-term oscillations but ignore longer term oscillations such as the 28-to-29-

194     month QBO cycle and the average 11.3-year solar cycle. A comparison of the two trend estimating

195     methods is shown in Fig. 3 for the entire 1979 to 2021 period showing that they agree quite closely, but

196     that the annual average method has slightly larger two standard deviations 2$\sigma$ than the MLR method.

197

198     The MLR method (Eqns. 1 and 2) are not applied poleward of the Arctic and Antarctic circles where

199     latitude dependent extended winter night periods occur. Additional latitude dependent terms of varying

200     periods would be needed for latitudes greater than 70$^O$. The annual average method does not have

201     these complications.

202
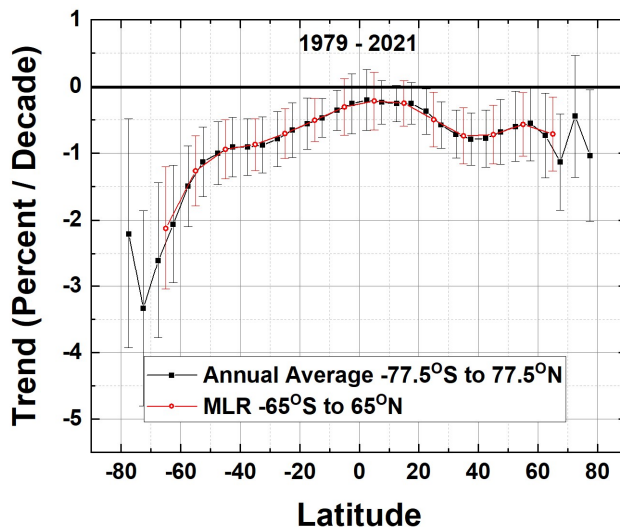
Fig. 3 The ozone trend $P_D(\theta)$ for the entire period 1979 – 2021 for two methods, MLR and Annual Average. The latitude grids for the two methods are offset to show the agreement in the trends and 2σ error bars.

203

204 The Fig. 3 estimation of linear long-term trends since 1979 is misleading, since ozone showed significant
205 annual declines until the mid-1990s and then increased slightly thereafter, meaning the average long-
206 term time series is non-linear. The usual procedure is to determine linear trends separately before and
207 after the turnaround dates $T_A$ (Weber et al., 2022). However, as is shown later, there is no single
208 turnaround date applicable to all the latitudes between 80°S and 80°N. Instead, there is a range
209 spanning 1994 to 1998.
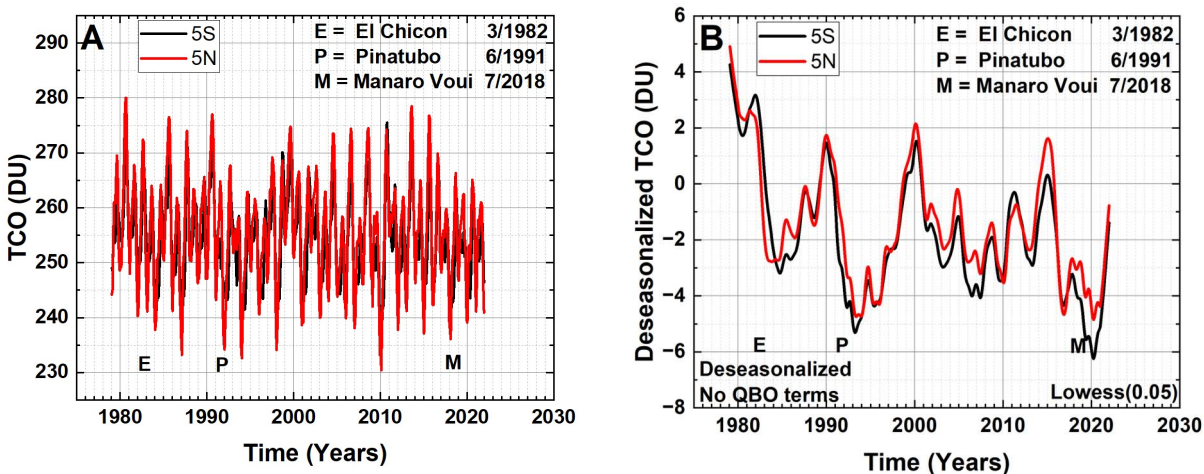
Fig. 4. A. $\Omega_{MOD}$ time series for $\theta = 5°N$ and 5°S. B. The deseasonalized TCO time series for $\theta = 5°N$ and 5°S without removing QBO effects (Eq. 1). The approximate dates are shown of volcanic eruptions that injected large amounts of SO₂ into the stratosphere leading to minima approximately 1 year later.

210

211 Figure 4A shows the $\Omega_{MOD}$ time series for 5$^O$S and 5$^O$N, and Fig. 4B the deseasonalized and smoothed
212 (Lowess(0.05)) $\Omega_{MOD}$ time series. After deseasonalizing, but not removing QBO effects (Eq. 1), both the
213 2.3-year QBO oscillation and the reduced ozone effects from volcanic eruptions, are shown in Fig. 4B.
214 Some volcanos (e.g., from El Chicon March 1982, Mt. Pinatubo June 1991, and Manaro Voui July 2018)
215 inject significant amounts of $SO_2$ into the lower stratosphere leading to the formation of aerosols that
216 reduce UV light and the production of ozone, especially in the equatorial region.

217 Figure 5 shows the Lowess(0.3) fits (black curves) to the $\Omega_{MOD}$ data for four sample latitude bands 55$^O$S,
218 45$^O$S, 55$^O$N, and 45$^O$N that tracks the longer-term changes in the $\Omega_{MOD}$ time series. Also shown are
219 examples of f = 0.1 (red) and f = 0.05 (blue dots). The Lowess(0.05) fit (blue dots) shows considerable
220 structure with a minimum in 1993 that is likely related to the Mt. Pinatubo eruption and a modest El
221 Nino effect in 1991-1992.The estimated values of $T_A$ for f = 0.1 and 0.05 can differ by 6 months from that
222 determined when f=0.3 because of short term oscillations. The Lowess(0.3) degree of smoothing
223 removes most of the short-term effects on ozone such as QBO and those from volcanic eruptions from
224 El Chichon (1982) and Mt. Pinatubo (1991), both well before the earliest estimated $T_A$ in 1994.
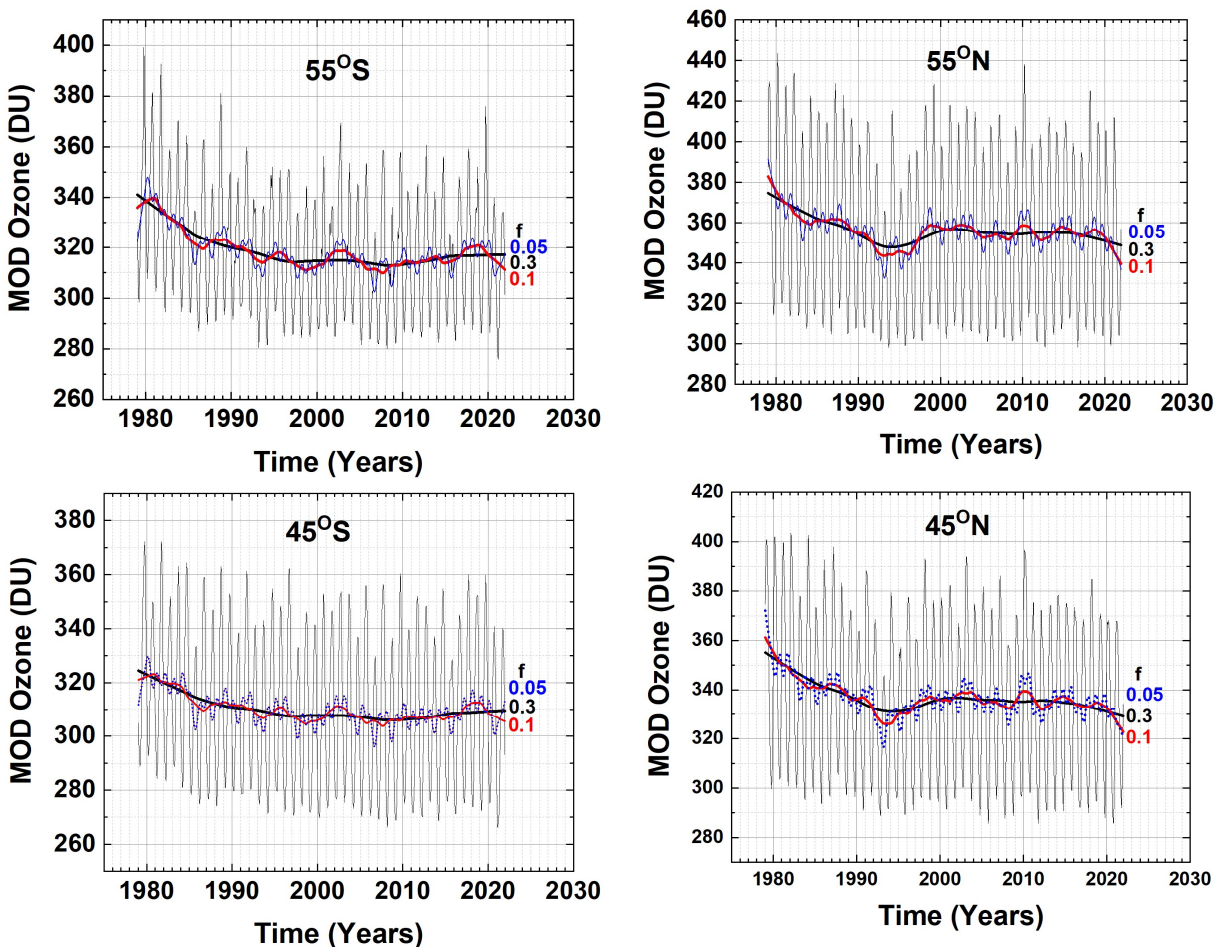
Fig. 5 $\Omega_{MOD}$ in four latitude bands and Lowess(0.3) fitting functions (f = 0.3, black lines). Examples of different f = 0.1 (Red) and 0.05 (blue dots) are shown at 45$^O$S and 45$^O$N. Note the slight downturn since 2010 in the Lowess(0.3) at 45$^O$N and 55$^O$N.

225  Figure 6 shows the Lowess(0.3) fits to the $\Omega_{MOD}$ data (1979 to 2021) for 16 latitude bands, $-75^O < \theta < 75^O$

226  on an expanded ozone scale. Each of the Lowess(0.3) plots for the various latitudes shows different

227  periods of ozone decrease and subsequent turnaround $T_A(\theta)$ after the mid-1990's. Use of expanded

228  ozone scales appears to show a sharp downturn after 2010 at some latitudes ($25^O$N to $75^O$N). As shown

229  later, the apparent downturns in the Lowess(0.3) fit to $\Omega_{MOD}$ after 2010 are not yet statistically

230  significant in trend estimates from $\Omega_{MOD}$ as an indicator of long-term ozone decrease.
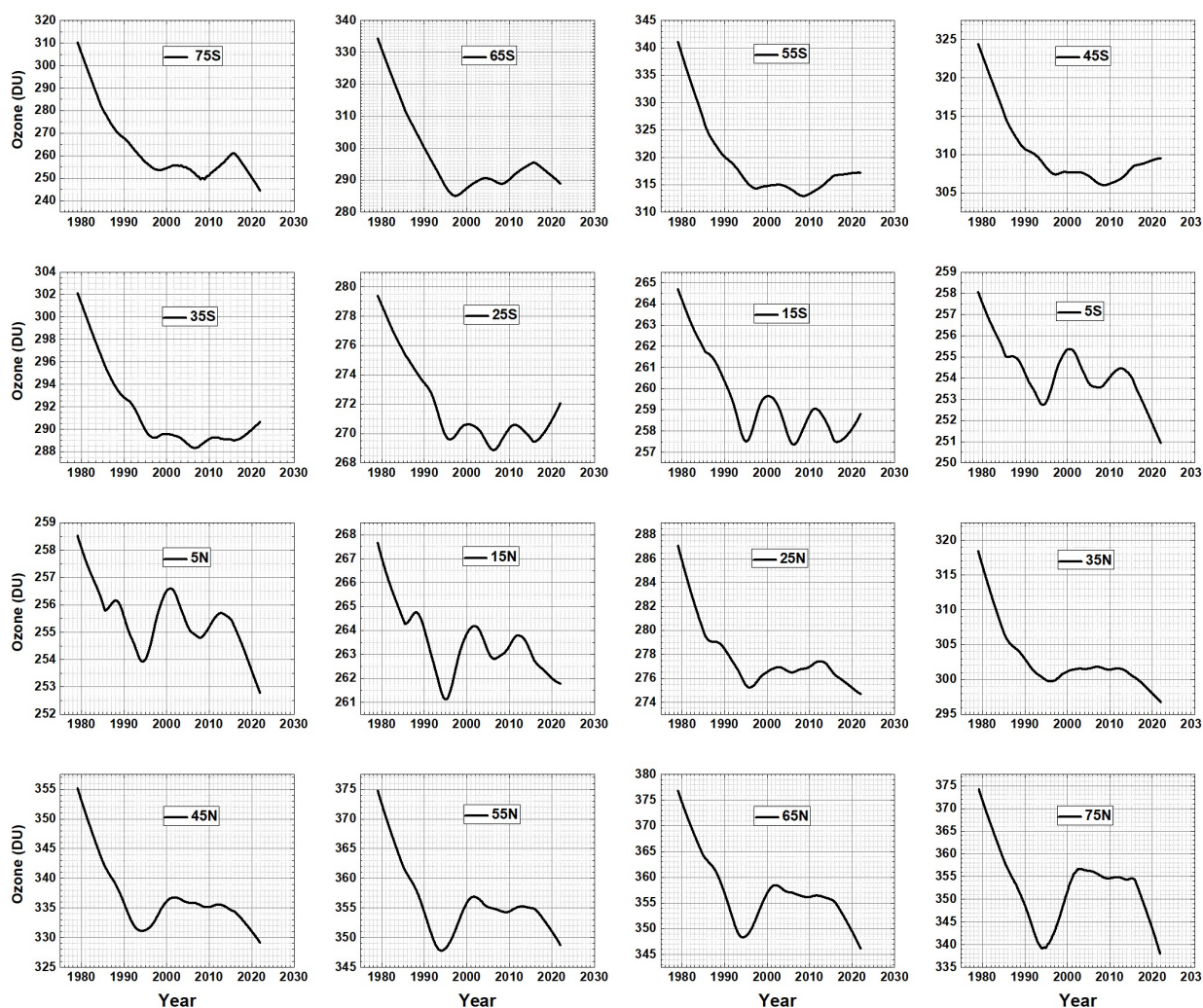
Fig. 6 Lowess(0.3) fits to the $\Omega_{MOD}$ data for 16 latitude bands used to determine $T_A(\theta)$. Note that the
ozone scale varies for each latitude.

231  Figure 7 shows the turnaround dates $T_A(\theta)$ that are obtained by taking the 1st derivatives of Fig. 6 data

232  and finding the zero-crossing time corresponding to the appropriate minimum value in Fig. 6. The exact

233  turnaround dates determined have a precision of ±0.1 years and an accuracy of ±0.5 years. The ±0.5

234  uncertainty does not affect the calculation of trends before and after the estimated $T_A(\theta)$. What is

235  interesting is that some of the turnaround dates in Fig. 7 are separated by over 4 years and are strongly

236  asymmetric between the hemispheres.  Figure 7 shows a near symmetry for early turnaround dates

237  1994-1996 for low latitudes between ±25$^O$ that corresponds to the Brewer-Dobson ozone upwelling

238  region (Brewer et al., 1926; Dobson, 1949; Butchart, 2014) where most of the ozone is created by

239  sunlight and then transported poleward. At poleward latitudes, the turnaround dates are quite

240  different, with a delayed date, 1997, at high SH latitudes (35$^O$S – 65$^O$S), 1998 at 75$^O$S compared to 1994

241  at high NH latitudes (45$^O$N to 75$^O$N).

242  The $T_A$ delay to 1997 for latitudes 35$^O$S – 65$^O$S follows the delayed recovery of ozone depletion within

243  the Spring Antarctic Ozone Hole (Solomon, 1990; Stone et al., 2021, their Fig. 3; Bodeker and Kremser,

244  2021, their Figs. 6 and 9) and backfilling (air exchange with lower latitude ozone-rich air) during the

245  summer months after the polar vortex winds break down in October – November.

246
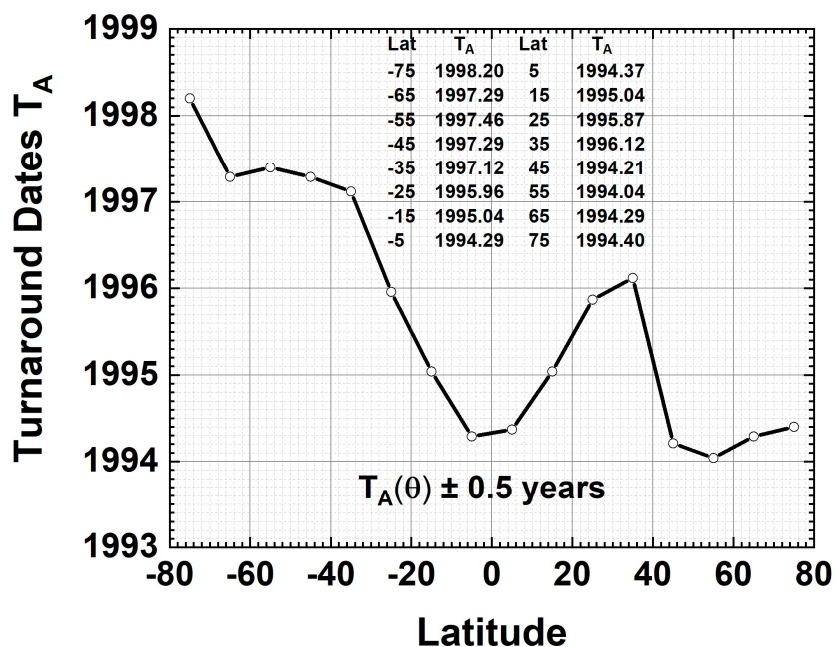
| Lat | $T_A$ | Lat | $T_A$ |
|-----|---------|-----|---------|
| -75 | 1998.20 | 5 | 1994.37 |
| -65 | 1997.29 | 15 | 1995.04 |
| -55 | 1997.46 | 25 | 1995.87 |
| -45 | 1997.29 | 35 | 1996.12 |
| -35 | 1997.12 | 45 | 1994.21 |
| -25 | 1995.96 | 55 | 1994.04 |
| -15 | 1995.04 | 65 | 1994.29 |
| -5 | 1994.29 | 75 | 1994.40 |

Fig 7 Turnaround dates $T_A(\theta)$ as a function of latitude from Fig.6 with an estimated accuracy of ±0.5 years based on the analysis in Fig. 5.

247

248  The general $T_A(\theta)$ pattern shown in Fig. 7 should appear in model calculations as a signature of the

249  combined effects of photochemistry, dynamics, and volcanic eruptions on the cessation of decreasing

250  ozone in the mid-1990s.
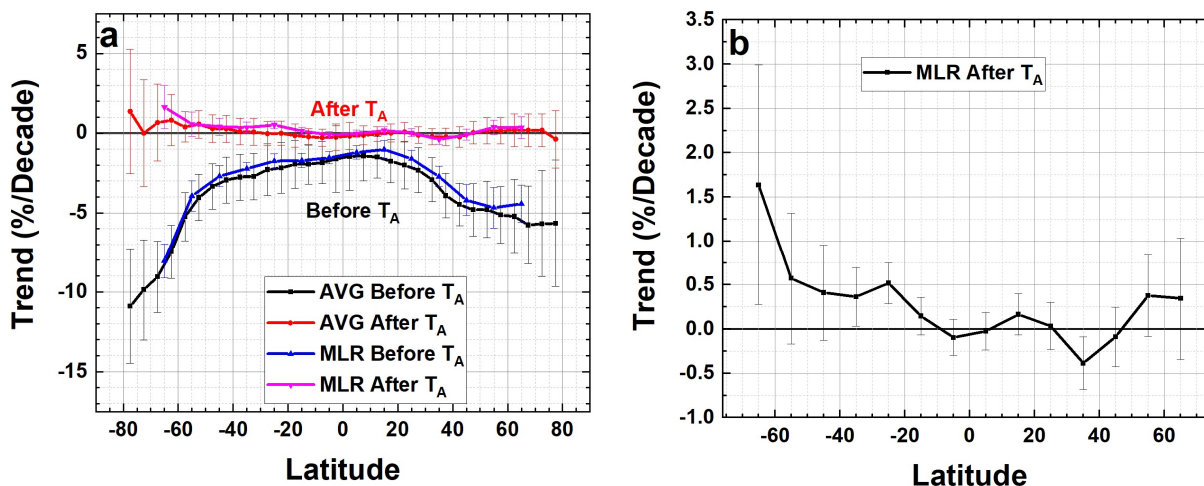
Fig. 8a Ozone trends $P_D(\theta)$ (percent per decade) using the MLR and Annual Average methods before and after $T_A(\theta)$. 6b A magnified version of the MLR estimated trends after $T_A$ with $2\sigma$ uncertainties.

251

252  Trends (linear slopes) $P_D(\theta)$ in percent per decade are estimated (Eqn. 3) for the separate periods before
253  and after $T_A(\theta)$ in each latitude band (Fig. 8) and for the entire period (Fig. 3). The linear slopes obtained
254  by the two methods, MLR and annual average closely agree (Figs. 3 and 8) with the annual average
255  method extended to polar latitudes (Fig. 8a). Table 1 contains the data from Figs. 8a and 8b.

Table 1 MLR Trends (%/decade) ± $2\sigma$

| Latitude | $P_D$ Before $T_A$ | $P_D$ After $T_A$ | Latitude | $P_D$ Before $T_A$ | $P_D$ After $T_A$ |
|---|---|---|---|---|---|
| -65 | -8.04±1.1 | 1.64±1.4 | 65 | -4.43±1.2 | 0.35±0.7 |
| -55 | -3.93±1.0 | 0.57±0.7 | 55 | -4.67±1.3 | 0.38±0.5 |
| -45 | -2.69±0.7 | 0.41±0.5 | 45 | -4.20±1.0 | -0.09±0.3 |
| -35 | -2.22±0.4 | 0.36±0.3 | 35 | -2.71±0.6 | -0.39±0.3 |
| -25 | -1.75±0.5 | 0.52±0.2 | 25 | -1.61±0.5 | 0.03±0.3 |
| -15 | -1.71±0.4 | 0.15±0.2 | 15 | -1.01±0.6 | 0.16±0.2 |
| -5 | -1.54±0.4 | -0.10±0.2 | 5 | -1.21±0.4 | -0.03±0.2 |

256

257  The latitude dependent trends derived by Weber et al. (2022) using 1996.5 as the approximate $T_A$ (their
258  Fig. 3) agree within error bars with the trends shown in Fig. 8 for all latitudes but they suggest $T_A$ = 2000
259  for the polar regions. The trends also agree within error bars with those in WMO (2022). As mentioned
260  earlier, the trend estimates are not very sensitive to the exact $T_A$, but the shape of $T_A(\theta)$ should be a
261  model validation marker contained in model calculations for all effects, not just ODSs.

262  The delayed (1997) Southern Hemisphere mid- and high-latitude values of $T_A$ are caused by coupling to
263  the increasing Antarctic spring ozone loss after 1979 until a recovery starting in about 1998-2000
264  (Solomon et al., 2016). The mid and high latitude, from 35°S to 65°S, delay is caused by the summer
265  mixing of ozone poor air from the Antarctic region with SH midlatitude ozone-rich air once the polar
266  vortex winds break down in November-December.

267 The asymmetry between the Arctic and Antarctic is caused by the lower winter Antarctic temperatures

268 (-80$^{O}$C) leading to the formation of low altitude clouds containing ice crystals along with the isolating

269 Antarctic polar vortex winds (Solomon et al., 2007; 2016). In the spring sunlight the ice and water

270 droplets (Tritscher, et al., 2021) release ODS and depletes ozone to a monthly average of about 155 DU.

271 During the summer, air exchange with ozone rich air from lower latitudes comes into the polar latitudes and

272 fills in the ozone layer above Antarctica (monthly average about 300 DU. Smaller but significant ozone losses

273 occurred in the Artic region caused by occasional low temperatures and ODSs. The Arctic does not

274 routinely have the low temperatures needed for winter ice clouds nor does it have the persistent

275 isolating polar vortex winds because of wave action forced by the land topography The latitude band at

276 75$^{O}$N (Fig.1) has the highest amount of monthly average winter ozone 450±25 DU that decreases to

277 290±20 DU monthly average during the summer that are comparable to mid-latitude values. The result

278 is earlier values of $T_A$ in the NH compared to the SH. The NH $T_A$ is earlier than the 1997 minimum in

279 stratospheric halogens (Weber et al., 2022; Newman et al., 2007). Note that $T_A$ is not the time of the

280 start of recovery, but rather the time for the end of rapid ozone decrease.

281

282 Before the SH $T_A$, total column ozone decreased at a rate of $P_D$= -10.9±3.6% at 77.5$^{O}$S and -8.0±1.1% per

283 decade at 65$^{O}$S, during the period from 1979 to 1997 with smaller decreases from 55$^{O}$S to 25$^{O}$S (Fig. 8a).

284 After the turnaround period $T_A$, ozone at 65$^{O}$S increased at $P_D$ = 1.6±1.4%/decade based on the MLR

285 method. After $T_A$, most other latitudes (Fig. 8b) show stationary ozone amounts within 2σ. In the NH the

286 decreases were smaller than in the SH before $T_A$ because of the absence of an Arctic ozone hole region.

287 At 77.5$^{O}$N was $P_D$ = -5.6±4%/decade and at 65$^{O}$N $P_D$ = -4.4±0.35 %/decade.

288 An analysis of ozone trends prior to the start of reliable satellite data in late 1978 showed that the

289 annual rate of ozone loss (%/Year) increased after 1978 (Staehelin et al., 2001).  Based on the first

290 derivatives of the data in Fig. 6, the maximum annual rate of ozone reduction occurred in 1979 and 1980

291 in the NH and SH (Fig. 9) except for 65$^{O}$N in 1992 where the rate of loss is -8.75%/Year.  The loss rates

292 range from -20.6 %/Year at 75$^{O}$S to 2.39 %/Year at 5$^{O}$N. A smaller loss rate occurred for 35$^{O}$N to 75$^{O}$N

293 where the loss rate is almost constant between 8%/Year and 10%/Year compared to the larger SH loss

294 rates caused by the presence of the springtime Antarctic ozone hole.
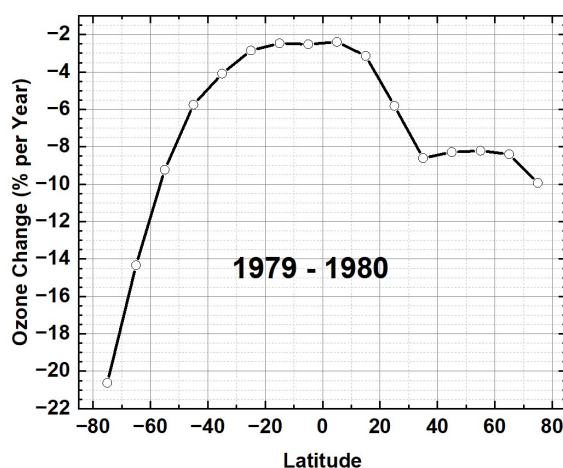
Fig. 9 The percent change in ozone per year in 1979 or 1980

295    The Lowess(0.3) plots in Fig. 6 suggest that $\Omega_{MOD}$ has been declining since approximately 2010 from $5^O$S
296    to $65^O$N but still increasing from $45^O$S to $65^O$S (Fig. 6). However, computing the trends (Fig. 10) from
297    $\Omega_{MOD}(t,\theta)$ using either the MLR (Eq. 1) or annual average methods suggest that the declines in ozone
298    from $25^O$S to $65^O$N are not yet significant at the $2\sigma$ level over the period 2010 – 2021.

299
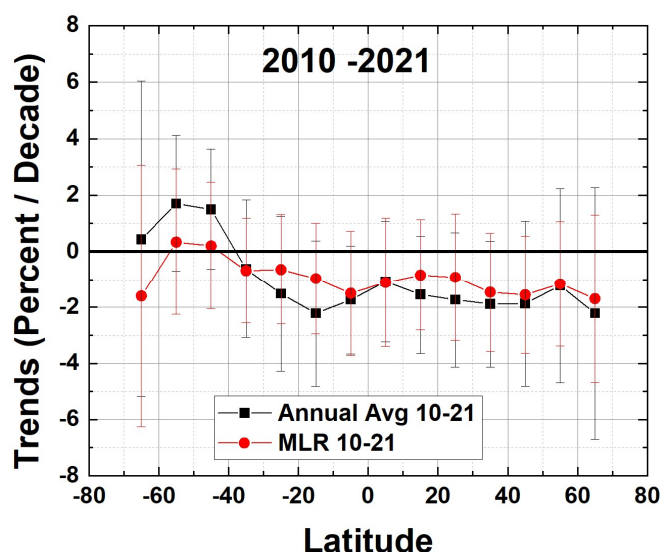
Fig. 10 Ozone trends $P_D(\theta)$ (Percent per Decade) for the period 2010 – 2021 for the Annual Average
and MLR methods applied to $\Omega_{MOD}(t,\theta)$.

300    Comparing deseasonalized $\Omega_{MOD}(t,\theta)$ with deseasonalized Microwave Limb Sounder MLS (see Appendix
301    Figs. A1, A2, and A3) Stratospheric Ozone from 2005 to 2021 shows small average (Lowess(0.3))
302    differences that are within ±1DU except for 2021 when the differences at both $65^O$S and $65^O$N are about
303    -2.5DU. This suggests that the calibrations of the later SBUV-2 and OMPS-NP instruments are stable. For
304    2016 to 2018, $\Omega_{MOD}$ is obtained from NOAA-19 SBUV plus OMPS-NP and from just OMPS-NP since 2018.
305    Figure A3 suggests that there was a decrease in tropospheric ozone in 2020 that may correspond to
306    reduced economic activity during the COVID-19 pandemic.

307    Age of air AoA is a measure of how long a parcel of air resides in the stratosphere after it leaves the
308    troposphere (Linz et al., 2016; Ploeger et al, 2021). A comparison of $T_A$ with AoA estimates from the
309    relatively inert tracer gas $CO_2$ (Fig. 11) for the altitude range near the ozone maximum (approximately
310    20 km) vs latitude (based on Waugh and Hall, 2002, their Fig. 6a and Ploeger et al, 2021 their Fig. 10a)
311    shows near symmetry between the hemispheres with the shortest AoA in the equatorial region. The
312    turnaround dates $T_A$ in Fig. 6 are also symmetric in the equatorial zone corresponding the upwelling
313    Brewer Dobson circulation and the smaller AoA. This suggests that the combined effects of chemistry
314    and dynamics on ozone amounts are similar between $\pm 25^O$. The precursors to ODS are also lifted into
315    the equatorial stratosphere and transported towards the polar regions (Newman et al., 2004; 2007)
316    where they can be photo-dissociated into ODS. Ozone at higher latitudes, NH and SH, with longer AoA,

317    will be dependent on transported ozone and ODS and their photochemistry, and especially the different

318    dynamics and chemistry in the Arctic and Antarctic regions.
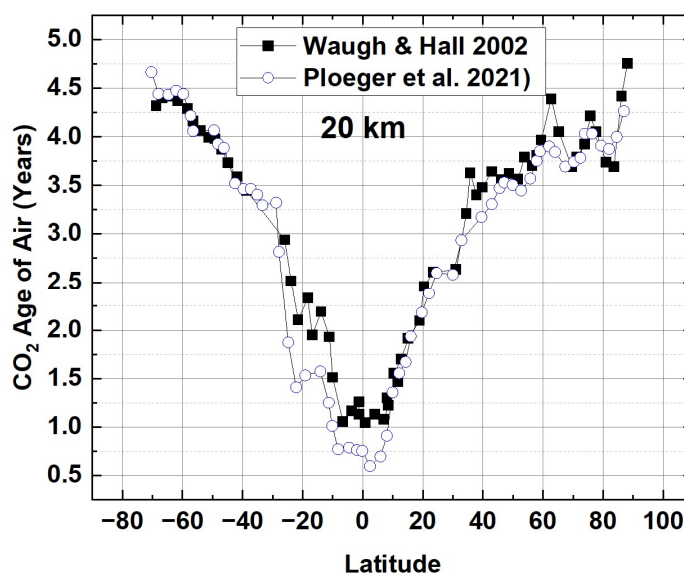
Fig. 11 Age of air derived from $CO_2$ data (Waugh and Hall, 2002; Ploeger et al., 2021)

319

320

321

322

323

324

325    **3.0 Summary**

326    The monthly averaged Merged Ozone Data set $\Omega_{MOD}$ ($2.5^O$ latitude bands, $77.5^OS$ to $77.5^ON$) from 1979

327    to 2021 were averaged into $10^O$ latitude bands $75^OS < \theta < 75^ON$. A smoothed $\Omega_{MOD}$ version based on

328    Lowess(0.3) was used to determine the approximate dates of the latitude dependent ozone end of

329    ozone decrease date $T_A(\theta)$ ranging from 1994 to 1998 with an error estimate of ±0.5 years. The

330    systematic hemispherically asymmetric latitude dependent pattern $T_A(\theta)$ should appear in atmospheric

331    models that combine the effects of volcanic eruptions, photochemistry, and dynamics in their estimate

332    of the end of ozone decrease. An examination of model studies that are part of CCMVal shows a nearly

333    uniform $T_A$ = 2000, suggesting that the several models' chemistry and dynamics including volcanic

334    effects are incomplete. The hemispheric asymmetry is caused by the formation of the annual Spring

335    Antarctic ozone (monthly spring average about 155 DU) hole with persistent isolating polar vortex winds

336    followed by the summer mixing with mid-latitude ozone rich air (December average about 300 DU). The

337    Arctic region does not form a large spring ozone hole, nor does it have sustained isolating polar vortex

338    winds. Instead at 75$^O$N (Fig. 1) it has the highest amount of monthly average winter ozone 450±25 DU

339    that decreases to 290±20 DU monthly average during the summer. Trends of ozone $P_D(\theta)$ in percent per

340    decade were computed before and after the latitude dependent $T_A(\theta)$ using two different methods, MLR

341    and annual averages, that closely agree over their mutual latitude range of validity, 65$^O$S to 65$^O$N. The

342    annual average method can extend into polar latitudes. The most dramatic rates of ozone loss were $P_D$ =

343    -10.9±3.6% decade at 77.5$^O$S and -8.0±1.1%/decade at 65$^O$S, which is about double the rate of loss of $P_D$

344    = -5.7±4 %/decade at 77.5$^O$N and -4.4±1.2% per decade at 65$^O$N. During the period after $T_A$ to 2021,

345    there has been a small increase at latitudes in the SH from 25$^O$S to 65$^O$S with the largest value being

346    1.6±1.4% per decade at 65$^O$S. Aside from the small increases in the SH region there has been no

347    statistically significant ozone recovery toward 1979 values, just an almost constant ozone amount after

348    $T_A(\theta)$. The largest annual rate of ozone decrease occurred near the beginning of the SBUV data record,

349    1979, showing large high latitude losses of -20.6 %/Year at 75$^O$S caused by the springtime Antarctic

350    ozone hole compared to a smaller Arctic loss of -9.9%/Year at 75$^O$N.  During the period 2010 to 2021,

351    there has been a small apparent decrease in ozone amount in $\Omega_{MOD}$ that is not yet statistically significant

352    at the 2-standard deviation level. A comparison between $\Omega_{MOD}$ and MLS stratospheric column ozone

353    shows small systematic negative differences in 2020 that mostly recovered in 2021 except near the

354    equator. This suggests that there is no statistically significant instrumental calibration drift between

355    $\Omega_{MOD}$ TCO and MLS stratospheric ozone.

356

357

358    **Appendix**

359    The MOD TCO data record since 2018 is obtained from OMPS-NP, which appears to show decreasing

360    TCO (Fig. 6). Because of this, the deseasonalized $\Omega_{MOD}$ are compared with MLS (Microwave Limb

361    Sounder) deseasonalized stratospheric column ozone for the period 2004 to 2021 to look for calibration

362    drifts in the $\Omega_{MOD}$ time series. The question addressed here is not the absolute agreement between $\Omega_{MOD}$

363    and the MLS mostly stratospheric ozone column, but rather if there is a systematic drift between the

364    two data sets after 2016. Figures A1 and A2 show that the difference between the two deseasonalized

365    time series for latitudes from 65$^O$S to 65$^O$N and for the entire period 2005 – 2021. Of interest is the

366    period 2016 to 2021 when $\Omega_{MOD}$ was derived using NOAA-19 SBUV plus OMPS-NP 2016 – 2018 and from

367    OMPS-NP since 2018.
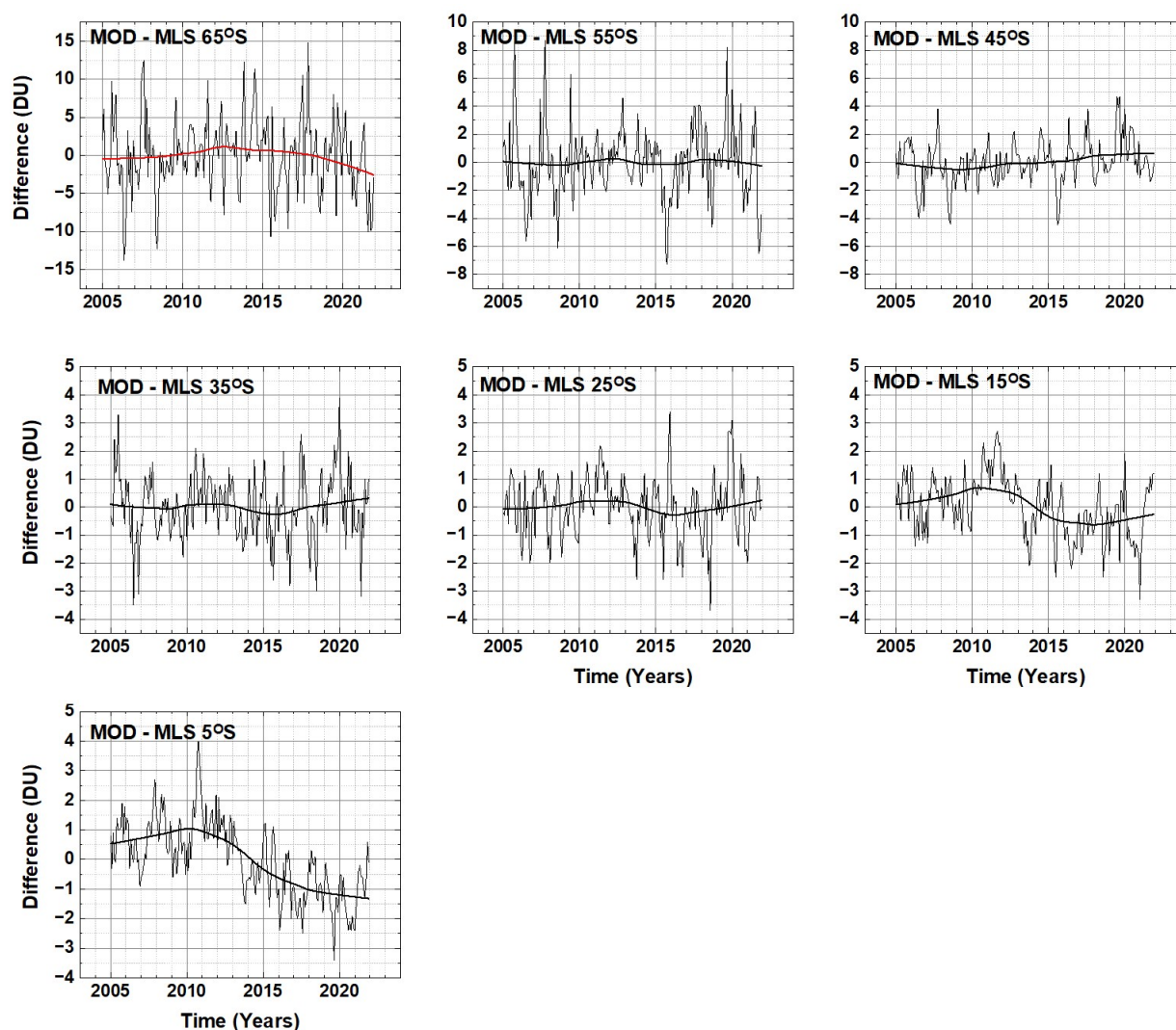
Fig. A1 A comparison of deseasonalized $\Omega_{MOD}$ with deseasonalized MLS stratospheric column ozone
for 65$^O$S to 5$^O$S.
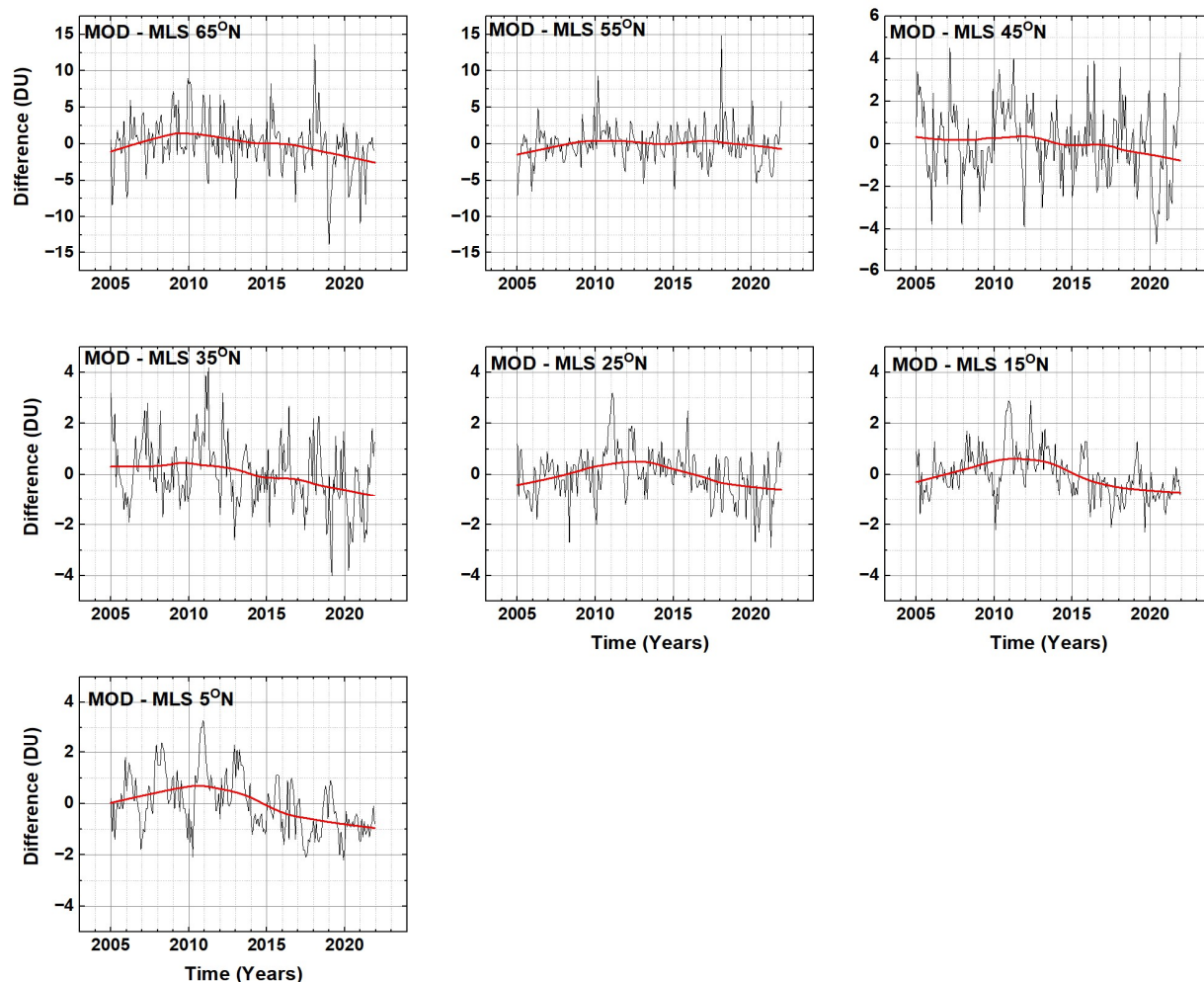
368

369

Fig. A2 A comparison of deseasonalized MOD total ozone with deseasonalized MLS stratospheric
column ozone for 5°N to 65°N. Variations of ±3DU are within the MOD merged record uncertainties.

370

371    The differences in Figs A1 and A2 between $\Omega_{MOD}$ and MLS since 2016 are not statistically significant at

372    the $2\sigma$ level. Variations of ± 3DU are within the $\Omega_{MOD}$ merged record uncertainties.

373

374    Since both MOD and MLS time series were deseasonalized, the mean values would be zero unless there

375    were changes in tropospheric ozone or instrument calibration drift. The differences are summarized in

376    Fig. A3 along with the $2\sigma'$, ($\sigma'$ = standard deviation from the mean) error bars estimated from the

377    average of each deseasonalized time series. In 2020 there appears to be a systematic change in <MOD −

378    MLS> that may be a reduction in tropospheric ozone amount of about 3 DU caused by the economic

379    slowdown associated with COVID-19 (Ziemke et al, 2022). The systematic change mostly recovered in

380    2021 (Fig. A3) except for -1DU near the equator (-5°S to 15°N).
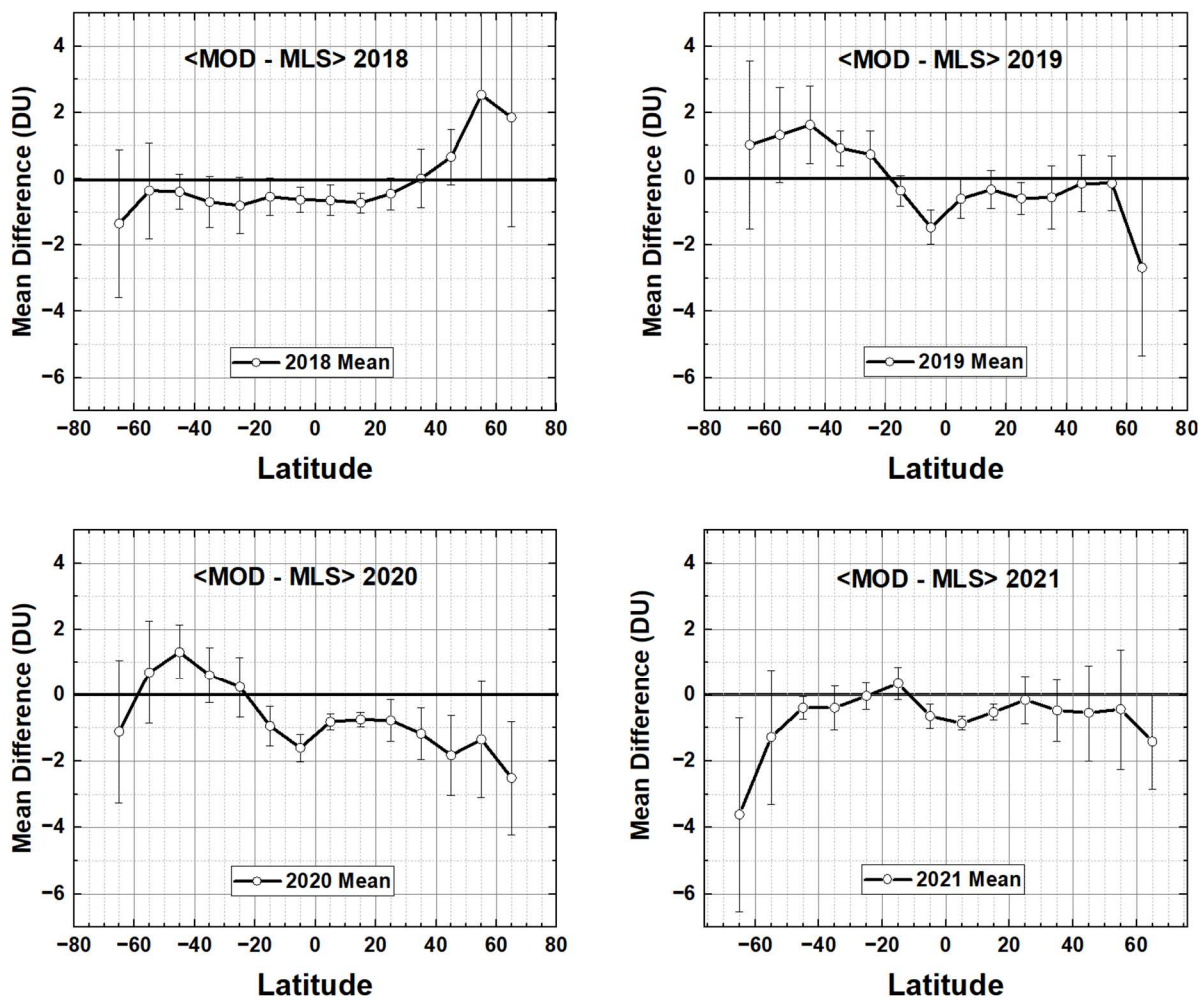
Fig. A3 Annual average <MOD – MLS> for the years 2018 to 2021. Error bars are 2σ′, where σ′ = standard error of the mean estimated from the average of the deseasonalized time series for each year shown in Figs. A1 and A2.

381

382

383   **4.0 References**

384   Bai, K., N.-B. Chang, R. Shi, H. Yu, and W. Gao, An intercomparison of multidecadal observational and
385   reanalysis data sets for global total ozone trends and variability analysis, J. Geophys. Res. Atmos., 122,
386   7119–7139, doi:10.1002/2016JD025835, 2017.

387   Bhartia, P. K. , R. D. McPeters, L. E. Flynn, S. Taylor, N. A. Kramarova, S. Frith, B. Fisher, and M. DeLand,
388   Solar Backscatter UV (SBUV) total ozone and profile algorithm. Atmos. Meas. Tech., 6, 2533–2548,
389   doi:10.5194/amt-6-2533-2013, 2013.

390   Bodeker, G. E. and Kremser, S.: Indicators of Antarctic ozone depletion: 1979 to 2019, Atmos. Chem.
391   Phys., 21, 5289–5300, https://doi.org/10.5194/acp-21-5289-2021, 2021.

392   Brewer, A. W., Evidence for a world circulation provided by the measurements of helium and water
393   vapour distribution in the stratosphere, Quarterly Journal of the Royal Meteorological Society. 75 (326):
394   351–363. Bibcode:1949QJRMS..75..351B. doi:10.1002/qj.49707532603. ISSN 1477-870X, 1949.

395   Crutzen, P. J. and Arnold, F.: Nitric acid cloud formation in the cold Antarctic stratosphere: a major cause
396   for the springtime "ozone hole", Nature, 342, 651–655, https://doi.org/10.1038/324651a0, 1986.

397   Dameris, Martin and Mark P. Baldwin, Impact of Climate Change on the Stratospheric Ozone Layer,
398   Stratospheric Ozone Depletion and Climate Change, Edited by Rolf Muller, Chapter 8, 214-252, Royal
399   Society of Chemistry 2012.

400   Dobson, G. M. B.; Harrison, D. N.; Lindemann, F. A., Measurements of the amount of ozone in the Earth's
401   atmosphere and its relation to other geophysical conditions, Proceedings of the Royal Society of London.
402   Series A, Containing Papers of a Mathematical and Physical Character. 110 (756): 660–693.
403   Bibcode:1926RSPSA.110..660D. doi:10.1098/rspa.1926.0040. 1926.

404   Butchart, N., The Brewer-Dobson circulation, Rev. Geophys.,52, 157–184, doi:10.1002/2013RG000448,
405   2014.

406   Cleveland, W.S., Robust Locally Weighted Regression and Smoothing Scatterplots, Journal of the
407   American Statistical Association, Vol. 74, pp. 829-836, https://doi.org/10.2307/2286407, 1979.
408
409   Cleveland, W.S. and Devlin, S.J., Locally Weighted Regression: An Approach to Regression Analysis by
410   Local Fitting," Journal of the American Statistical Association, Vol. 83, pp. 596-610,
411   DOI: 10.1080/01621459.1988.10478639 1988.
412
413   DeLand, M. T., S. L. Taylor, L. K.Huang, and B. L. Fisher, Calibration of the SBUV version 8.6 ozone data
414   product, Atmos. Meas. Tech., 5, 2951–2967, doi:10.5194/amt-5-2951-2012, 2012.
415
416   Eyring, V., Cionni, I., Bodeker, G. E., Charlton-Perez, A. J., Kinnison, D. E., Scinocca, J. F., Waugh, D. W.,
417   Akiyoshi, H., Bekki, S., Chipperfield, M. P., Dameris, M., Dhomse, S., Frith, S. M., Garny, H., Gettelman,
418   A., Kubin, A., Langematz, U., Mancini, E., Marchand, M., Nakamura, T., Oman, L. D., Pawson, S., Pitari, G.,
419   Plummer, D. A., Rozanov, E., Shepherd, T. G., Shibata, K., Tian, W., Braesicke, P., Hardiman, S. C.,
420   Lamarque, J. F., Morgenstern, O., Pyle, J. A., Smale, D., and Yamashita, Y.: Multi-model assessment of

421 stratospheric ozone return dates and ozone recovery in CCMVal-2 models, Atmos. Chem. Phys., 10,
422 9451–9472, https://doi.org/10.5194/acp-10-9451-2010, 2010a.
423
424 Eyring, V. T. Shepherd and D. Waugh (Eds.)SPARC, SPARC CCMVal Report on the Evaluation of
425 Chemistry-Climate Models. , SPARC Report No. 5, WCRP-30/2010, WMO/TD – No. 40,
426 https://www.sparc-climate.org/publications/sparc-reports/, 2010b.
427
428 Frith, S. M., N. A. Kramarova, R. S. Stolarski, R. D. McPeters, P. K. Bhartia, and G. J. Labow, Recent
429 changes in total column ozone based on the SBUV Version 8.6 Merged Ozone Data Set, J. Geophys. Res.
430 Atmos., 119, 9735-9751, doi:10.1002/2014JD021889, 2014.

431 Frith, S. M., Stolarski, R. S., Kramarova, N. A., and McPeters, R. D.: Estimating uncertainties in the SBUV
432 Version 8.6 merged profile ozone data set, Atmos. Chem. Phys., 17, 14695–14707,
433 https://doi.org/10.5194/acp-17-14695-2017, 2017.

434 Frith, S. M., Bhartia, P. K., Oman, L. D., Kramarova, N. A., McPeters, R. D., and Labow, G. J.: Model-based
435 climatology of diurnal variability in stratospheric ozone as a data analysis tool, Atmos. Meas. Tech., 13,
436 2733-2749, https://doi.org/10.5194/amt-13-2733-2020, 2020.
437
438 Dhomse, Sandip, Kinnison, Douglas, Chipperfield, Martyn, Cionni, Irene, Hegglin, M., Abraham, N.,
439 Akiyoshi, Hideharu & Archibald, Alex & Bednarz, Ewa & Bekki, Slimane & Braesicke, Peter & Butchart,
440 Neal, Dameris, M., Deushi, Makoto, Frith, Stacy, Hardiman, Steven, Hassler, Birgit, Horowitz, Larry, Hu,
441 Rong-Ming, Zeng, Guang, Estimates of Ozone Return Dates from Chemistry-Climate Model Initiative
442 Simulations. Atmospheric Chemistry and Physics Discussions, 1-40. 10.5194/acp-2018-87, 2018.
443
444 Guttman, I., Linear Models, An Introduction, 358 pp., Wiley-Interscience, New York, 1982.

445 Herman, J.R., R. McPeters, D. Larko, Ozone depletion at northern and southern latitudes derived from
446 January 1979 to December 1991 Total Ozone Mapping Spectrometer data, 98, 13783-12793
447 https://doi.org/10.1029/93JD00601, 1993.

448 Khosrawi, F., Urban, J., Pitts, M. C., Voelger, P., Achtert, P., Kaphlanov, M., Santee, M. L., Manney, G. L.,
449 Murtagh, D., and Fricke, K.-H.: Denitrification and polar stratospheric cloud formation during the Arctic
450 winter 2009/2010, Atmos. Chem. Phys., 11, 8471–8487, https://doi.org/10.5194/acp-11-8471-2011,
451 2011.

452 Linz, Marianna, R. Alan Plumb, Edwin P. Gerber, Aditi Sheshadri, The Relationship between Age of Air
453 and the Diabatic Circulation of the Stratosphere. J. Atmos. Sci., 73, 4507-4518, doi: 10.1175/JAS-D-16-
454 0125.1, 2016.

455 McPeters, R. D., P. K. Bhartia, D. Haffner, G. J. Labow, and L. Flynn, The version 8.6 SBUV ozone data
456 record: An overview, J. Geophys. Res. Atmos., 118, 8032-8039, doi:10.1002/jgrd.50597., 2013.

457 Newman, P.A., S. R. Kawa, E. R. Nash, On the size of the Antarctic ozone hole, Geophys. Res. Lett., 1-4,
458 31, doi:10.1029/2004GL020596, 2004.

459    Newman, P. A., Daniel, J. S., Waugh, D. W., and Nash, E. R., A new formulation of equivalent effective
460    stratospheric chlorine (EESC), Atmos. Chem. Phys., 7, 4537–4552, https://doi.org/10.5194/acp-7-4537-
461    2007, 2007.

462    Oldenborgh, Geert Jan van, Harry Hendon, Timothy Stockdale, Michelle L'Heureux, Erin Coughlan de
463    Perez, Roop Singh, and Maarten van Aalst, Defining El Niño indices in a warming climate, Environ. Res.
464    Lett. 16 044003, DOI 10.1088/1748-9326/abe9ed, 2021.

465    Randel, W. J., and J. B. Cobb, Coherent variations of monthly mean total ozone and lower stratospheric
466    temperature, J. Geophys. Res., 99, 5433--5447, DOI:10.1029/93JD03454, 1994.
467
468    Robertson, F., Revell, L. E., Douglas, H., Archibald, A. T., Morgenstern, O., & Frame, D., Signal-to-noise
469    calculations of emergence and de-emergence of stratospheric ozone depletion. Geophysical Research
470    Letters, 50, 1-11, e2023GL104246. https://doi.org/10.1029/2023GL10424, 2023.

471    Solomon, S., Garcia, R. R., Rowland, F. S., and Wuebbles, D. J.: On the depletion of Antarctic ozone,
472    Nature, 321, 755–758, https://doi.org/10.1038/321755a0, 1986.

473    Solomon, S., Stratospheric ozone depletion: a review of concepts and history, Rev. Geophys., 37, 275–
474    316,  https://doi.org/10.1029/1999RG900008, 1999.

475    Solomon, S., Portmann, R. W., & Thompson, D. W., Contrasts between Antarctic and Arctic ozone
476    depletion. Proceedings of the National Academy of Sciences, 104(2), 445-449.
477    https://doi.org/10.1073/pnas.0604895104, 2007.

478    Solomon, Susan, Diane J. Ivy, Doug Kinnison, Michael J. Mills, Ryan R. Neely, Iii, And Anja Schmidt,
479    Emergence of healing in the Antarctic ozone layer, Vol 353, 269-274 DOI: 10.1126/science.aae0061,
480    2016.

481    Staehelin, J., N. Harris,  C. Appenzeller, and J. Eberhard, Ozone trends: A review, REV GEOPHYS., 39,231-
482    290, 10.1029/1999RG000059, 2001.

483    Stolarski R. D., P. Bloomfield, R. D. McPeters, and J. R. Herman, Total ozone trends deduced from
484    Nimbus 7 TOMS data, Geophys., Res., Lett., 18, https://doi.org/10.1029/91GL01302, 1991.

485    Stolarski R, Bojkov R, Bishop L, Zerefos C, Staehelin J, Zawodny J. Measured trends in stratospheric
486    ozone, Science, Apr 17;256(5055):342-9. doi: 10.1126/science.256.5055.342. PMID: 17743110, 1992.
487
488    Stone, K. A., Solomon, S., and Kinnison, D. E., On the identification of ozone recovery. Geophysical
489    Research Letters, 45, https://doi.org/10.1029/2018GL077955, 2018.
490
491    Stone KA, Solomon S, Kinnison DE, Mills MJ. On Recent Large Antarctic Ozone Holes and Ozone Recovery
492    Metrics. Geophys Res Lett. 2021 Nov 28;48(22):e2021GL095232. doi: 10.1029/2021GL095232. Epub
493    2021 Nov 18. PMID: 35864979; PMCID: PMC9286815.
494

495  Strahan, S. E., and Douglass, A. R., Decline in Antarctic ozone depletion and lower stratospheric chlorine
496  determined from Aura Microwave Limb Sounder observations. Geophysical Research Letters, 45, 382–
497  390. https://doi.org/10.1002/2017GL074830, 2018.
498
499  Tritscher, I., Pitts, M. C., Poole, L. R.,Alexander, S. P., Cairo, F., Chipperfield, M. P., et al. (2021). Polar
500  stratospheric clouds: Satellite observations, processes, and role in ozone depletion. Reviews of
501  Geophysics, 59, e2020RG000702. https://doi.org/10.1029/2020RG000702, 2021.
502  Velders, G. J., & Andersen, S. O. (2018). The Montreal Protocol on Substances that Deplete the Ozone
503  Layer and its amendments: An overview. Air Pollution and Health, 11-28, 2018.
504  Wallace, J. M., R. L. Panetta, and J. Estberg, Representation of the equatorial stratospheric quasi-biennial
505  oscillation in EOF phase space, J. Atmos. Sci., 50, 1751--1762, https://doi.org/10.1175/1520-
506  0469(1993)050<1751:ROTESQ>2.0.CO;2, 1993.
507
508  Weatherhead, E. C., Reinsel, G. C., Tiao, G. C., Meng, X.-L., Choi, D., Cheang, W.-K., Keller, T., DeLuisi, J.,
509  Wuebbles, D. J., Kerr, J. B., Miller, A. J., Oltmans, S. J., and Frederick, J. E.:  Factors affecting the
510  detection of trends: Statistical considerations and applications to environmental data, 103,17149–
511  17161, https://doi.org/10.1029/98JD00995, 1998.
512
513  Waugh, D.W. and Hall, T.M., Age of stratospheric air: theory, observations, and models, Rev. of
514  Geophys., 40,1-10, doi:10.1029/2000RG000101, 2002.
515  Weber, Mark, Carlo Arosio, Melanie Coldewey-Egbers, Vitali E. Fioletov, Stacey M. Frith, Jeannette D.
516  Wild, Kleareti Tourpali, John P. Burrows, and Diego Loyola, Global total ozone recovery trends attributed
517  to ozone-depleting substance (ODS) changes derived from five merged ozone datasets,
518  https://doi.org/10.5194/acp-22-6843-2022, ACP, 22, 6843–6859, 2022.
519
520  World Meteorological Organization (WMO), Scientific Assessment of Ozone Depletion: 2022, GAW
521  Report No. 278, 509 pp., WMO, Geneva, 2022.
522  Ziemke, Jerry R. Luke D. Oman, Sarah A. Strode, Anne R. Douglass, Mark A. Olsen, Richard D.
523  McPeters, Pawan K. Bhartia, Lucien Froidevaux, Gordon J. Labow, Jacquie C. Witte, Anne M.
524  Thompson, David P. Haffner, Natalya A. Kramarova, Stacey M. Frith, Liang-Kang Huang, Glen R.
525  Jaross, Colin J. Seftor, Mathew T. Deland, Steven L. Taylor, Trends in global tropospheric ozone inferred
526  from a composite record of TOMS/OMI/MLS/OMPS satellite measurements and the MERRA-2 GMI
527  simulation, Atmospheric Chemistry and Physics, 10.5194/acp-19-3257-2019, **19**, 5, (3257-3269), 2019.
528  Ziemke, J. R., N. A. Kramarova, S. M. Frith, L.-K. Huang, D. P. Haffner, K. Wargan, L. N. Lamsal, G. J.
529  Labow, R. D. McPeters, and P. K. Bhartia, NASA satellite measurements show global-scale reductions in
530  tropospheric ozone in 2020 and again in 2021 during COVID-19, Geophys. Res. Lett.,
531  49,  https://doi.org/10.1029/2022GL098712, 2022.

532

533  **Author contribution**:

534 Jay Herman is responsible for writing the text, the annual integral trend calculations, and all the
535 figures. Jerald Ziemke supplied the MLR trend calculations and the comparison with MLS. Richard
536 McPeters supplied the MOD ozone as a continuous function of time from 1979 to 2021 for each
537 latitude band.

538 **Data Availability**
539 The original data used are publicly available in an ASCII format.
540 https://acd-ext.gsfc.nasa.gov/Data_services/merged/
541 and processed data in Excel format
542 https://avdc.gsfc.nasa.gov/pub/DSCOVR/JayHerman/MOD_Ozone_Trends/
543
544
545 **Competing interests**:
546 The authors declare that they have no conflict of interest.

547
548
549
550
551 **Acknowledgements**:
552 The authors want to acknowledge the contribution and help of Stacey Frith for compiling the SBUV
553 and OMPS-NP data sets to produce the long ozone data record. She also reviewed the paper and
554 added some important corrections.
555

556 **Figure Captions**

557 Fig. 1 Left: The zonally and monthly averaged $\Omega_{MOD}$ data set 1979 – 2021 and -77.5$^O$ to 77.5$^O$. Right: Time
558 and zonal averaged ozone and its maxima and minima 1979 – 2021. Error bars are 1 standard deviation
559 ±1σ.

560 Fig. 2 The latitude average residual term from Eq. 1 in percent 100 <R(t,q$_i$)/W$_{MOD}$(t,q$_i$)> The black line is
561 the Lowess(0.1) fit (Cleveland, 1979) to the R(t,q) with an average error estimate of ±2%. The light-
562 colored lines are each latitude's R(t,q) in a hemisphere 0$^O$ < θ < 65$^O$.

563 Fig. 3 The ozone trend $P_D(\theta)$ for the entire period 1979 – 2021 for two methods, MLR and Annual
564 Average. The latitude grids for the two methods are offset to show the agreement in the trends and 2σ
565 error bars.

566 Fig. 4. A.  $\Omega_{MOD}$ time series for θ = 5$^O$N and 5$^O$S.  B. The deseasonalized TCO time series for θ = 5$^O$N and
567 5$^O$S without removing QBO effects (Eq. 1). The approximate dates are shown of volcanic eruptions that
568 injected large amounts of $SO_2$ into the stratosphere leading to minima approximately 1 year later.

569 Fig. 5 $\Omega_{MOD}$ in four latitude bands and Lowess(0.3) fitting functions (f = 0.3, black lines). Examples of
570 different f = 0.1 (Red) and 0.05 (blue dots) are shown at 45$^O$S and 45$^O$N. Note the slight downturn since
571 2010 in the Lowess(0.3) at 45$^O$N and 55$^O$N.

572 Fig. 6 Lowess(0.3) fits to the $\Omega_{MOD}$ data for 16 latitude bands used to determine $T_A(\theta)$. Note that the
573 ozone scale varies for each latitude.

574 Fig 7 Turnaround dates $T_A(\theta)$ as a function of latitude from Fig.6 with an estimated accuracy of ±0.5
575 years based on the analysis in Fig. 5.

576 Fig. 8a Ozone trends $P_D(\theta)$ (percent per decade) using the MLR and Annual Average methods before and
577 after $T_A(\theta)$. 6b A magnified version of the MLR estimated trends after $T_A$ with 2σ uncertainties.

578 Fig. 9 The percent change in ozone per year in 1979 or 1980

579 Fig. 10 Ozone trends $P_D(\theta)$ (Percent per Decade) for the period 2010 – 2021 for the Annual Average and
580 MLR methods applied to $\Omega_{MOD}$(t,θ).

581 Fig. 11 Age of air derived from $CO_2$ data (Waugh and Hall, 2002; Ploeger et al., 2021)

582 Fig. A1 A comparison of deseasonalized $\Omega_{MOD}$ with deseasonalized MLS stratospheric column ozone for
583 65$^O$S to 5$^O$S.

584 Fig. A2 A comparison of deseasonalized MOD total ozone with deseasonalized MLS stratospheric column
585 ozone for 5$^O$N to 65$^O$N.  Variations of ±3DU are within the MOD merged record uncertainties.

586     Fig. A3 Annual average <MOD – MLS> for the years 2018 to 2021. Error bars are $2\sigma'$, where $\sigma' =$

587     standard error of the mean estimated from the average of the deseasonalized time series for each year

588     shown in Figs. A1 and A2.

589